

of virtual walls, we can produce functionality on microchips that is difficult to realize by other methods. For example, concentrating samples in microfluidic systems is nontrivial. Methods reported include sample stacking using "isoelectric focusing" (30) and on-chip solid phase extraction (31). The virtual walls provide an intuitive method to concentrate liquids on microchips. Virtual walls can also mimic the function of lungs by exchanging components between liquid and gas phases. In combination with in situ-constructed stimuli-responsive hydrogel components (25, 32), more complex functions could be added to realize even greater control in microfluidic systems. We believe that the approaches we describe provide enhanced functionality and design flexibility that expand the toolbox for the design and fabrication of microfluidic systems.

References and Notes

1. M. Freemantle, *Chem. Eng. News* 77 (no. 8), 27 (1999).
2. M. A. Unger et al., *Science* 288, 113 (2000); J. Fahr- enberg et al., *J. Micromech. Microeng.* 5, 169 (1995); C. Goll et al., *J. Micromech. Microeng.* 6, 77 (1996); X. Yang, C. Grosjean, Y. C. Tai, C. M. Ho, *Sens. Actuators A* 64, 101 (1998).
3. D. J. Harrison et al., *Science* 261, 895 (1993).
4. H. Salimi-Moosavi, T. Tang, D. J. Harrison, *J. Am. Chem. Soc.* 119, 8716 (1997).
5. G. Beni, M. A. Tenan, *J. Appl. Phys.* 52, 6011 (1981).
6. B. S. Gallardo et al., *Science* 283, 57 (1999).
7. D. E. Kataoka, S. M. Troian, *Nature* 402, 794 (1999).
8. M. A. Burns et al., *Proc. Natl. Acad. Sci. U.S.A.* 93, 5556 (1996).
9. A. W. Adamson, *Physical Chemistry of Surfaces* (Wiley, New York, ed. 5, 1990).
10. J. C. Mcdonald et al., *Electrophoresis* 21, 27 (2000).
11. K. Handique, B. P. Gogoi, D. T. Burke, C. H. Mastran- gles, M. A. Burns, *Proc. SPIE* 3224, 185 (1997).
12. E. Delamarque, A. Bernard, H. Schmid, B. Michel, H. Biebuyck, *Science* 276, 779 (1997).
13. K. Ichimura, S.-K. Oh, M. Nakagawa, *Science* 288, 1624 (2000).
14. H. Gau, S. Herminghaus, P. Lenz, R. Lipowsky, *Science* 283, 46 (1999).
15. A. A. Darhuber, S. M. Troian, S. M. Miller, *J. Appl. Phys.* 87, 7768 (2000).
16. A. D. Strook et al., *Phys. Rev. Lett.* 84, 3314 (2000).
17. G. T. A. Kovacs, *Micromachined Transducer Source- book* (McGraw-Hill, Boston, 1998).
18. B. H. Weigl, P. Yager, *Science* 283, 346 (1999).
19. P. J. A. Kenis, R. F. Ismagilov, G. M. Whiteside, *Science* 285, 83 (1999).
20. S. Takayama et al., *Proc. Natl. Acad. Sci. U.S.A.* 96, 5545 (1999).
21. A. Ulman, *An Introduction to Ultrathin Organic Films* (Academic Press, Boston, 1991).
22. A. Ulman, *Chem. Rev.* 96, 1533 (1996).
23. B. Zhao, D. Mulkey, W. J. Brittain, Z. Chen, M. D. Foster, *Langmuir* 15, 6856 (1999).
24. We used hexadecane (Aldrich, 99%) as a solvent to form SAMs of trichlorosilanes on silica substrates. Contact angle measurement showed that SAMs with full coverages were formed on glass substrates in less than 2 min.
25. D. J. Beebe et al., *Nature* 404, 588 (2000).
26. Hexadecane and the solution of trichlorosilane in hexadecane [0.5 weight-to-volume percent (w/v %)] were pumped into channels by two syringe pumps (Harvard Apparatus PHD 2000 Programmable). Sy- ringes were connected to pipette tips fixed to chan- nels by silicone tubing (Helix Medical, 0.040" ID/ 0.085" OD). Because the reactivity of trichlorosilanes is high, solvent was always introduced into the chan- nel before the silane solution to eliminate the for-

27. A pipette tip with inner diameters of 8 mm at the bottom and 6 mm at the top was fixed onto the channels. The maximum pressure that virtual walls can withstand was determined by gradually adding deionized water into the pipette and then measuring water height when a bulge developed.
28. The surface free energy of Rhodamine B dilute solu-

- tion is lower than that of deionized water, resulting in a lower maximum pressure.
29. D. H. Rich, S. K. Gurwara, *J. Am. Chem. Soc.* 97, 1575 (1975); V. N. R. Pillai, *Synthesis (Germany)* (1980), p. 1.
30. S. C. Jacobson, M. Ramsey, *Electrophoresis* 16, 481 (1995).
31. R. D. Oleschuk, L. L. Shultz-Lockyear, Y. Ning, D. J. Harrison, *Anal. Chem.* 72, 585 (2000).
32. D. J. Beebe et al., *Proc. Natl. Acad. Sci. U.S.A.* 97, 13488 (2000).
33. Supported by a grant from the Defense Advanced Research Projects Agency (MTO F30602-00-1-0570) (A. Lee, Program Manager). We acknowledge J. Orlicki for assisting with the images and Q. Yu for help in generating the photomasks.

8 November 2000; accepted 4 January 2001

The Detection of Large HNO₃-Containing Particles in the Winter Arctic Stratosphere

D. W. Fahey,^{1,3*} R. S. Gao,¹ K. S. Carslaw,⁴ J. Kettleborough,⁵ P. J. Popp,^{1,3} M. J. Northway,^{1,3} J. C. Holecek,^{1,3} S. C. Ciciora,^{1,3} R. J. McLaughlin,¹ T. L. Thompson,¹ R. H. Winkler,¹ D. G. Baumgardner,⁶ B. Gandrud,⁷ P. O. Wennberg,^{8,9} S. Dhaniala,⁸ K. McKinney,⁸ Th. Peter,¹⁰ R. J. Salawitch,^{8,9} T. P. Bui,¹² J. W. Elkins,² C. R. Webster,¹¹ E. L. Atlas,⁷ H. Jost,^{12,13} J. C. Wilson,¹⁴ R. L. Herman,¹¹ A. Kleinböhl,¹⁵ M. von König¹⁵

Large particles containing nitric acid (HNO₃) were observed in the 1999/2000 Arctic winter stratosphere. These in situ observations were made over a large altitude range (16 to 21 kilometers) and horizontal extent (1800 kilometers) on several airborne sampling flights during a period of several weeks. With diameters of 10 to 20 micrometers, these sedimenting particles have significant potential to denitrify the lower stratosphere. A microphysical model of nitric acid trihydrate particles is able to simulate the growth and sedimentation of these large sizes in the lower stratosphere, but the nucleation process is not yet known. Accurate modeling of the formation of these large particles is essential for understanding Arctic denitrification and predicting future Arctic ozone abundances.

Polar stratospheric cloud (PSC) particles play a well-recognized role in the chemical loss of stratospheric ozone over the Antarctic and Arctic regions in winter/early spring (1–3). PSCs are formed at low temperatures (<200 K), characteristic of the winter stratosphere, through the co-condensation of water and HNO₃. Heterogeneous reactions on PSC particles produce active chlorine species. The sedimentation of PSC particles irreversibly removes HNO₃ (denitrification) and water (dehydration) from the lower stratosphere. Denitrification slows the return of chlorine to its inactive forms and, hence, enhances ozone destruction in a winter/spring season (4–6).

Evidence of denitrification is abundant in both polar stratospheres from both in situ and remote observations (2, 7–11). Denitrifica- tion is most intense over the Antarctic region, where large fractions of available NO_y are irreversibly removed from the stratosphere

each winter. NO_y is the sum of principal reactive nitrogen species, of which HNO₃, NO, NO₂, N₂O₅, and ClONO₂ are important in the lower stratosphere (12). In principle, denitrification must involve the sedimenta- tion of large HNO₃-containing particles (13, 14), but important details of the process have not been confirmed by observation or fully described theoretically. The concentration of denitrifying particles must generally be much less than that of the background liquid sulfate aerosols (0.1-μm diameter). Too little con- densable material (HNO₃, H₂O) exists in the stratosphere to allow all particles to grow simultaneously to sizes sufficient for rapid sedimentation, particularly when ice does not form.

Here we report observations in the Arctic winter stratosphere of a newly identified class of large HNO₃-containing particles. The par- ticles were observed between January and

March 2000 with three instruments on board the NASA ER-2 high-altitude aircraft as it flew in the lower stratosphere inside the Arctic vortex (Fig. 1) (15, 16). Two instruments measured NO_y and HNO₃, respectively, in both the gas phase and in aerosols, and one measured the size and number concentration of individual particles. The presentation here is based primarily on the NO_y instrument, which has two independent measurement channels in order to distinguish sizes greater and less than ~2 μm in diameter ("front" and "rear" NO_y data, respectively) (Fig. 2).

The most extensive population of large particles was observed at aircraft cruise altitudes (16 to 21 km) on 20 January 2000 during a flight between Kiruna, Sweden, and the North Pole (Figs. 1 and 2). Isolated peaks in the front NO_y data (Fig. 2C) at the beginning and end of the flight represent the sampling of individual HNO₃-containing particles. Throughout most of the flight, however, the front NO_y data show a continuous series of peaks (Fig. 2D) due to the sampling of a larger number concentration of particles. The mass-equivalent sphere diameter associated with an individual particle peak can be calculated if typical PSC particle compositions are assumed (17). The most likely solid phases to form below 200 K are nitric acid trihydrate (HNO₃·3H₂O) (NAT) and nitric acid dihydrate (HNO₃·2H₂O) (NAD) (3, 18, 19). Single large particles are unlikely to be liquid supercooled ternary solution (STS) composed of HNO₃, H₂O, and H₂SO₄ (20). For a single particle composed of NAT, the relation between diameter *D* and the recorded NO_y value is $D (\mu\text{m}) = 4.7 [\text{NO}_y (\text{ppbv})]^{1/3}$ (ppbv, parts per billion by volume). Thus, the data in Fig. 2 suggest that particles of sizes much greater than 2 μm in diameter were present

over large horizontal regions (1800 km) in the center of the Arctic vortex. The presence of large particles is confirmed by the direct HNO₃ and aerosol size measurements (16).

The NO_y observations raise three questions. First, how can the size and number concentration be determined for these large HNO₃-containing particles? Second, do these

Fig. 1. Map of the ER-2 ground track on the flight of 20 January 2000 (yellow line) beginning in Kiruna, Sweden (67°N), reaching a maximum latitude of 89°N, and returning to Kiruna. The temperature field is shown by color shading and labeled contours (in K) on the 430 K isentropic surface (~19 km) at 1200 UTC on 20 January. The edge of the Arctic vortex (red contour) is defined by a potential vorticity value of $2.1 \times 10^{-5} \text{ K m}^2 \text{ kg}^{-1} \text{ s}^{-1}$. The thick portion of the yellow line indicates that portion of the flight track where large particles were present.

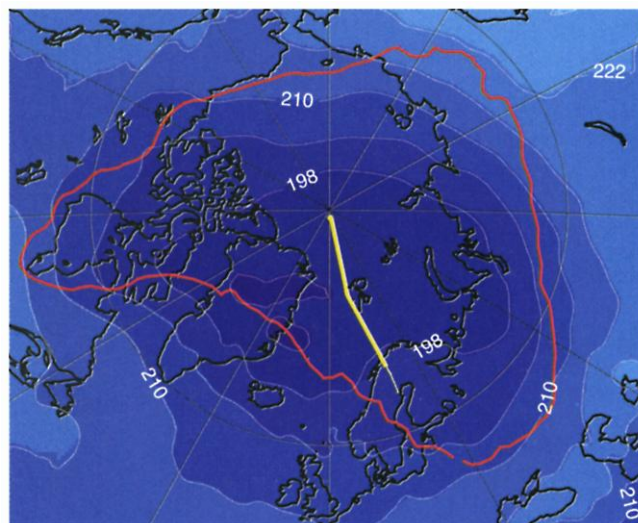
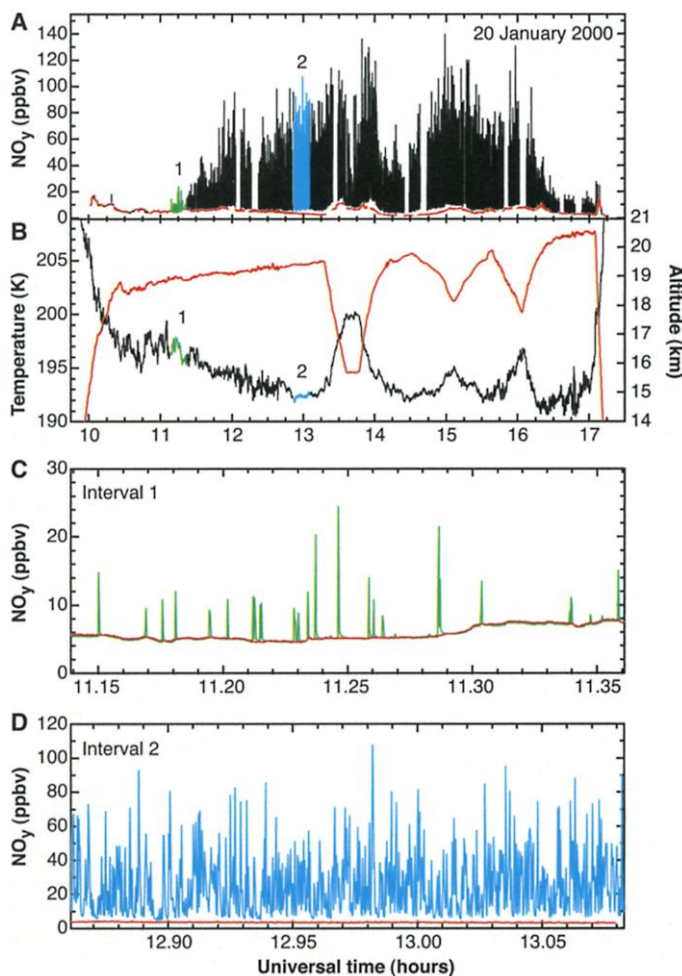


Fig. 2. Recorded data from the ER-2 flight of 20 January versus universal time (UT) corresponding to the flight track in Fig. 1. NO_y values from the front (black) and rear (red) inlets are shown for the entire flight in (A). Temperature (black) and altitude (red) are shown in (B). The 800-s intervals labeled in (A) as "1" (green) and "2" (blue) are expanded in (C) and (D), respectively. The data gaps in (A) correspond to instrument calibration periods. The aircraft speed is 0.2 km s⁻¹. The two NO_y measurements are made with inlets located front and rear, respectively, on a particle separator attached to the aircraft fuselage (12, 43). Air entering the front NO_y inlet contains particles of all sizes present, whereas air entering the rear NO_y inlet is inertially stripped of particles with diameters greater than ~2 μm. The separator does not affect the sampling of gas-phase species. Sampled particles are heated to 40°C along with sampled air, ensuring the release of condensed HNO₃ (and H₂O). Released HNO₃ is measured together with gas-phase HNO₃ through catalytic conversion to NO, which is subsequently detected by NO/O₃ chemiluminescence (12).



¹Aeronomy Laboratory, ²Climate Monitoring and Diagnostics Laboratory, National Oceanic and Atmospheric Administration, Boulder, CO 80305, USA. ³Cooperative Institute for Research in Environmental Sciences, University of Colorado, Boulder, CO 80309, USA. ⁴School of the Environment, University of Leeds, Leeds LS2 9JT, UK. ⁵Rutherford Appleton Laboratory, Chilton, Didcot, OX 11 0QX, UK. ⁶Universidad Nacional Autónoma de México, Centro de Ciencias de la Atmósfera, Ciudad Universitaria, 04510 Mexico DF, Mexico. ⁷National Center for Atmospheric Research, Boulder, CO 80307, USA. ⁸Division of Geology and Planetary Sciences, ⁹Division of Engineering and Applied Science, California Institute of Technology, Pasadena, CA 91125, USA. ¹⁰Laboratorium für Atmosphärenphysik, Eidgenössische Technische Hochschule Zürich, CH-8093 Zürich, Switzerland. ¹¹NASA Jet Propulsion Laboratory, Pasadena, CA 91109, USA. ¹²NASA Ames Research Center, Moffett Field, CA 94035, USA. ¹³Bay Area Environmental Research Institute, San Francisco, CA 94122, USA. ¹⁴Department of Engineering, University of Denver, Denver, CO 80208, USA. ¹⁵Institute of Environmental Physics, University of Bremen, D-28334 Bremen, Germany.

*To whom correspondence should be addressed. E-mail: fahey@al.noaa.gov

particles contribute substantially to denitrification in the lower stratosphere? Third, how do these particles form in the lower stratosphere? To address the first question, we used a statistical simulation to determine the size and number concentration of particles sampled in interval 2 (Fig. 2). This 800-s interval was chosen because the average NO_y signal due to particles is large (21 ppbv) and has a relatively constant standard deviation. This suggests that the size distribution is also relatively invariant over this interval. The large-

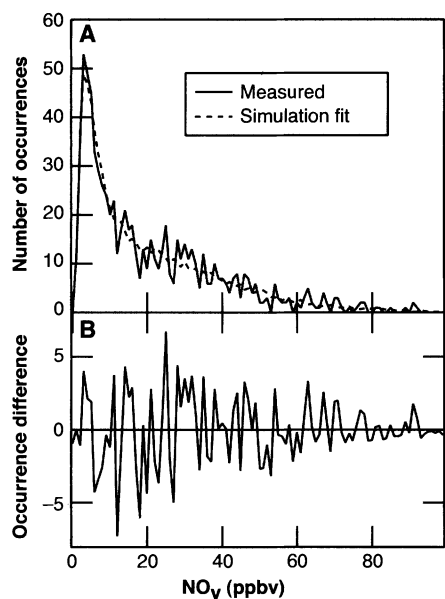


Fig. 3. Results from the statistical simulation of NO_y difference values for interval 2 on 20 January. The occurrence histogram of NO_y difference values is shown in (A) for the 800 s of observations in interval 2 (solid line) and for 20,000 s in the simulation (dashed line). The larger simulation period reduces the variability in the simulation histogram in (A). The best-fit size distribution for interval 2 is given by the Gaussian functions N ($\# \text{ cm}^{-3} \mu\text{m}^{-1}$) = $2.8 \times 10^{-3} \exp[-20(D - 3.5)^2] + 4.3 \times 10^{-5} \exp[-0.083(D - 14.5)^2]$, where D is the particle diameter in μm (Fig. 4). Gaussian functions are chosen for convenience to represent particle populations at large and small sizes. Lognormal distributions could also be used. The simulated time series is produced by superimposing the released HNO_3 from all particle sizes and averaging it to 1-s intervals to match the sampling period of the NO_y instrument. The differences between the simulated and observed histograms are shown in (B). The differences are very sensitive to the features of the large mode. For example, shifting the large mode by $\pm 2 \mu\text{m}$ would produce significantly larger differences in (B) than shown. The small-size mode in Fig. 4 is required to match the histogram peak below 10 ppbv. The exact number and size of these smaller particles is more uncertain than for the larger particles. The small mode represents only a subset of particles present in the atmosphere below a 5- μm diameter. The histogram comparison is not sensitive to the presence of additional particles with sizes between the two size modes and with concentrations $< 10^{-5}$ particles $\text{cm}^{-3} \mu\text{m}^{-1}$.

particle NO_y signal is defined as the difference between the front and rear NO_y values and thus only includes NO_y associated with particles larger than 2 μm (Fig. 2). The statistical simulation accounts for the sampling of more than one particle in any 1-s sampling period and for the spreading of HNO_3 from an individual particle over more than a single

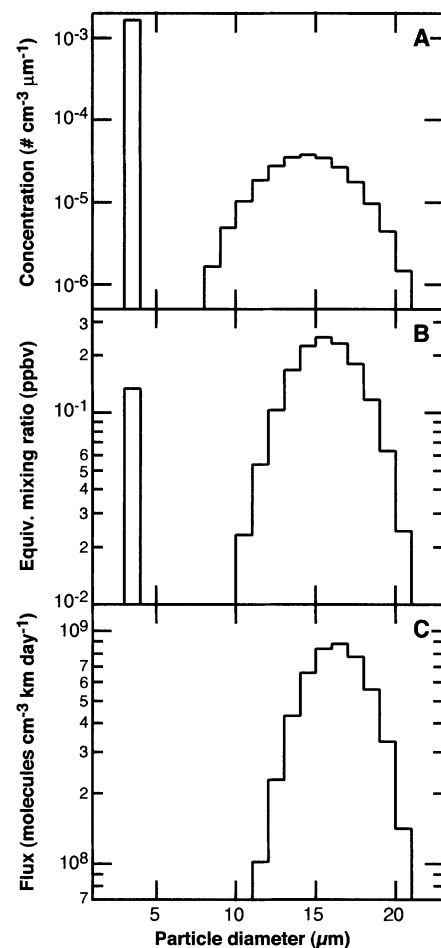


Fig. 4. Results from the statistical simulation of NO_y values in interval 2 on 20 January. Panels show (A) the adjusted best-fit size distribution and number concentration, (B) the equivalent gas-phase mixing ratio of HNO_3 derived from the distribution, and (C) the derived flux of HNO_3 at 60 hPa (~ 19.5 km). The size distribution is given by the Gaussian functions in the caption of Fig. 3 adjusted to account for size-dependent sampling efficiency. The adjustments, which are in addition to a basic particle enhancement factor of 12.8 (72), vary from +30 to -10% over the size range and are calculated with a fluid dynamical model of the particle separator. The concentration integral of the large (small) mode is $2.3 \times 10^{-4} \text{ cm}^{-3}$ ($2 \times 10^{-5} \text{ cm}^{-3}$), with an estimated uncertainty of $\pm 30\%$. The lower limit of the vertical axis in (A) corresponds to the detection of a single particle over the 800-s observation period. The total gas-phase HNO_3 of the large (small) mode is 1.5 ppbv (0.2 ppbv). The HNO_3 flux of the combined distribution is 5×10^9 molecules $\text{cm}^{-3} \text{ km day}^{-1}$ or 2.2 ppbv km day^{-1} at 60 hPa.

1-s period (20). The NO_y time series was simulated by sampling a randomly distributed population of NAT particles along a notional flight track (Fig. 3). The number concentrations in each size interval are the adjustable parameters. The representativeness of the size distribution was determined by comparing the occurrence histogram of NO_y difference values with that from the simulated time series (Fig. 3). The best-fit size distribution was found by iteratively adjusting the distribution to minimize the difference histogram (Fig. 3B).

Two particle size modes, shown in Fig. 4, are required in our analysis to reproduce the occurrence histogram of interval 2. The larger mode has a mean diameter of 14.5 μm and a total number concentration of $2.3 \times 10^{-4} \text{ cm}^{-3}$. This mode produces most of the NO_y values above 10 ppbv in Fig. 3. The smaller mode at 3.5 μm has a number concentration of $\sim 2 \times 10^{-5} \text{ cm}^{-3}$ and is well separated from the larger mode by size bins with fewer particles. For these concentrations, a large particle is sampled by the front inlet approximately every 1.8 s, and a small particle is sampled every 0.2 s on average. The HNO_3 mass contained in the large mode is equivalent to an ambient gas-phase value of 1.5 ppbv along the flight track (Fig. 4B). The mass of the more numerous smaller mode is ~ 0.2 ppbv. Because the simulation is of the difference between the two NO_y measurements, the small mode in Fig. 4 represents only the largest sizes in one or more particle modes present in the atmosphere below a diameter of 5 μm (16). With lower fall speeds, these smaller modes form separately from the large-particle mode and nearer to the sampling altitude, and may include particles composed of STS.

To answer the second question, whether these particles contribute substantially to stratospheric denitrification, we note that the existence of large HNO_3 -containing particles means that denitrification has already occurred because particles sediment during the growth process. An instantaneous sedimentation flux of HNO_3 can be calculated for the simulated size distribution by convolving the fall speed and NO_y content for each particle size in 1- μm size intervals (Fig. 4C). The fall speed of a 14- μm spherical particle is $\sim 1.5 \text{ km day}^{-1}$ at 18 to 19 km (21). The HNO_3 flux for interval 2 is 5×10^9 molecules $\text{cm}^{-3} \text{ km day}^{-1}$ (2.6 ppbv km day^{-1}) at flight altitudes. The flux values for many other flight intervals on 20 January are similar on the basis of average NO_y difference values and occurrence histograms for these intervals. Thus, some denitrification must have occurred above flight altitudes in the vortex before 20 January in order to produce the large particles observed on that day in many widely distributed air parcels. The denitrifi-

REPORTS

cation of the Arctic vortex in a given winter depends on the spatial and temporal extent of sedimenting particle populations. If a flux value of 2.6 ppbv km day⁻¹ were to be sustained for a period of only days near 20 km in a column model, a significant fraction (~50%) of available HNO₃ above 20 km would be removed.

Between 20 January and 7 March, large HNO₃-containing particles were present in six additional sampling flights inside the Arctic vortex. The number and spatial extent of particles observed on these later flights were significantly less than those observed on 20 January. As the stratosphere warmed above NAT saturation temperatures by mid-March, large particles no longer appeared in the NO_y data. On these later flights, two sampling periods contained particle populations that were notably different from those observed on 20 January. Both periods occurred at altitudes between 15 and 16 km. On 31 January, a 10-s burst of large particles was sampled with an average NO_y difference value many times that of interval 2. With diameters estimated to be near 20 μm, the instantaneous HNO₃ flux far exceeds that found in interval 2. From the 3 February flight, the analysis of an 800-s interval shows a population of primarily 12-μm-diameter particles with concentrations near 10⁻³ cm⁻³ and an estimated flux comparable to that of interval 2.

Denitrification was widespread in the 1999/2000 Arctic winter, as estimated with the rear NO_y measurements and the NO_y-N₂O correlation as a reference (7, 22). Denitrification exceeded 50% in many sampled air parcels in the 16- to 21-km cruise altitude range throughout the vortex in the January to March period, including most of the 20 January flight. Widespread denitrification was also found in satellite observations (23). The unusually low stratospheric temperatures in this Arctic winter, beginning in December, increased the likelihood of PSC formation and vortex denitrification (24). The different large-particle populations described here all contributed to vortex denitrification through their formation and sedimentation. It is likely, given the low winter temperatures, that similar populations present before 20 January further contributed to observed denitrification.

In answer to the third question, as to how these large particles form in the lower stratosphere, we note that NAT particles above 10 μm in diameter found between 16 and 21 km must begin their growth and sedimentation at substantially higher altitudes. The altitude displacement is a function of growth rate and sedimentation velocity. To demonstrate how the large particle sizes in Fig. 4 evolved after nucleation, we calculated sedimentation trajectories backward in time for particles ob-

served in interval 2 (Fig. 5). Growing particles are advected by atmospheric winds and, hence, will be transported horizontally and vertically while they gravitationally sediment. The trajectory calculations take into account air parcel advection simultaneously with particle growth and sedimentation. The time evolution of particle size, pressure altitude, temperature, and NAT supersaturation ratio for particle sizes between 6 and 18 μm in diameter shows several important features (Fig. 5). First, the trajectories for all sizes terminate (reach zero size) in NAT-supersaturated air, indicating that the observed sizes are consistent with atmospheric and microphysical constraints of the trajectory model. Air masses encountered by particles must have temperatures that cause NAT supersaturation (short times at higher temperatures can be survived if particles are large enough). Second, growth of the largest particle requires 6 days and an ~6-km vertical displacement at temperatures below NAT saturation values. Third, the trajectories terminate at different altitudes, temperatures, and NAT supersaturation values. The horizontal locations of the termination points also vary (25). These preliminary results suggest that there are no obvious preferred locations or satura-

tion conditions for nucleating the NAT particles observed in interval 2. The accumulation of HNO₃ in large particles in interval 2 causes some denitrification over the range of terminal altitudes. Finally, the trajectory temperatures at the start of particle growth (188 to 194 K) are above ice saturation by a few degrees. However, given the uncertainty in the meteorological analyses and atmospheric variability, ice saturation could have occurred along or near the trajectories and possibly played a role in particle nucleation. Particle trajectories also were calculated forward in time for interval 2. The results show that a 20-μm particle would continue to grow for another day, reach a maximum diameter of 22 μm at 150 hPa, and then evaporate (causing nitrification) within a few hours. Many instances of nitrification (NO_y in excess of the reference value) were observed in the vortex on the ER-2 flights.

Isolated particles sampled in interval 1 were significantly smaller than the mean size found in interval 2 (Fig. 2). The results of a similar particle trajectory analysis for interval 1 are consistent with the observed maximum size of ~13 μm in diameter. Although the trajectory analysis can account for such differences in size between different locations, it

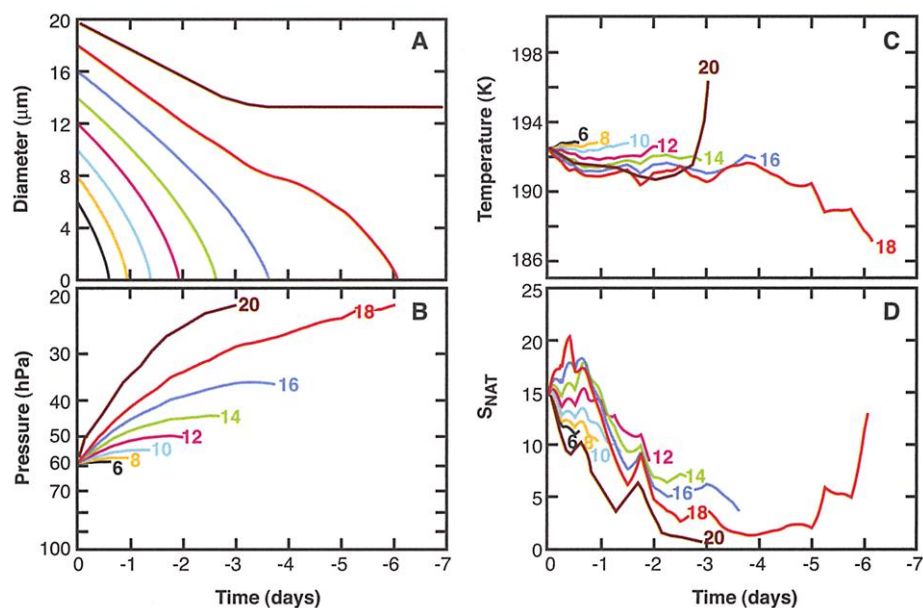


Fig. 5. Sedimentation trajectory calculations for different size particles present in interval 2 of Fig. 2. Trajectories simultaneously account for sedimentation, growth, and advection of a particle backward in time from interval 2. Trajectories for various particle sizes between 6 and 18 μm in diameter at day 0 are shown with colored lines and labeled by diameter. The results for (A) size, (B) pressure, (C) temperature, and (D) HNO₃ supersaturation ratio with respect to NAT (S_{NAT}) at the particle location are shown versus time (in days). The trajectories terminate where the particle diameter reaches zero. The trajectories were calculated by superimposing the particle vertical displacements due to sedimentation onto isentropic trajectories calculated with analyzed winds from the European Centre for Medium-Range Weather Forecasts. An H₂O mixing ratio of 5 ppmv and an HNO₃ mixing ratio of 7 ppbv were assumed, the latter being consistent with remote sounding observations (7 to 9 ppbv averaged above ER-2 altitudes) in mid-January 2000 (26). Temperatures remain above ice saturation for all particles. Particles with diameters greater than ~18 μm (or 20 μm at 9 ppbv HNO₃) had diameters greater than zero at the point where their trajectories exceeded the NAT equilibrium temperature and, thus, could not be present in interval 2 if growth began at the zero-size limit.

cannot account for differences in observed particle number concentrations. Concentrations depend on the spatial and temporal variation of the particle nucleation process throughout the low-temperature regions of the vortex.

The sensitivity of large-particle formation to available HNO₃ and temperatures near ice saturation was examined with a one-dimensional model of aerosol growth and sedimentation (Fig. 6) (20). The results show that the maximum NAT particle size that could be found at ER-2 cruise altitudes (50 to 70 hPa) is near 20 μm in diameter for average HNO₃ values observed above ER-2 altitudes in mid-January (7 to 9 ppbv) (26). This maximum size is consistent with the NO_y observations (Fig. 4). At ER-2 sampling altitudes, a 25% reduction in available HNO₃ causes a 10% reduction in particle size (20 to 18 μm). Similarly, a 2 K increase in temperature reduces the particle diameter by <10%. Particle sizes >22 μm can only be produced with a uniform abundance of >10 ppbv HNO₃ above the aircraft, which is greater than that observed in January to March 2000. These and larger particles were therefore unlikely to be found at or above a 60-hPa pressure altitude (~19 km).

The particle growth model results show that denitrification by large particles is mostly controlled by the kinetics of HNO₃ vapor deposition onto particles at conditions away from thermodynamic equilibrium of the NAT condensed phase. This is a result of the low number concentrations of particles and their large fall speeds. The assumption that NAT particles are in equilibrium, as used in various ways in most current atmospheric model simulations of denitrification, will lead to incorrect simulations of denitrification. Thus, the observations and analysis presented here suggest

a need for fundamental changes in the vortex-scale modeling of denitrification. Representative modeling of denitrification will require accounting for particle growth along sedimentation trajectories, thereby convolving the temporal and spatial coordinates of the winter vortex in a detailed way.

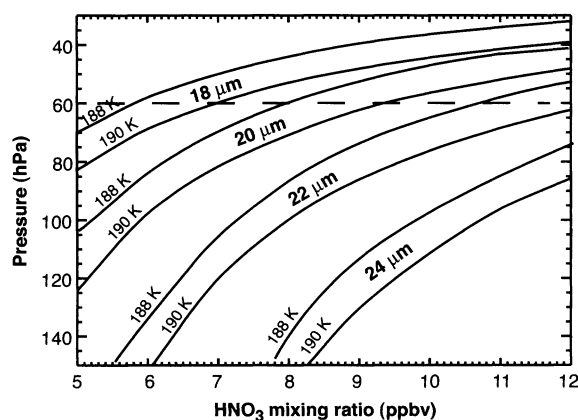
Critically lacking for representative modeling of denitrification is an identified and verified nucleation process for this newly identified class of large particles. If nucleation involves preexisting particles, the process must effect a high selectivity because background aerosol number concentrations are near 10 cm⁻³ in the lower stratosphere ($D > 0.008 \mu\text{m}$) (27, 28), whereas the computed large-particle concentration in interval 2 is near 10⁻⁴ cm⁻³. Selectivity is the key to the growth of the large-particle population observed here and their denitrification potential. If all available background particles grew and took up typical stratospheric HNO₃ amounts as NAT (or NAD), the average particle diameter would be <1 μm, and the sedimentation speed of individual particles would be <0.1 km day⁻¹ (13). This speed is not adequate to explain significant denitrification as observed in both polar regions (13, 14, 29). Selectivity could be the consequence of (i) a very low freezing rate of background particles to form NAT (or NAD) at temperatures below ~197 K (30, 31), (ii) the unique composition of a few nuclei (32, 33), or (iii) ice formation (10, 13, 34) possibly involving lee-wave clouds (10).

Antarctic satellite observations show that denitrification occurs before dehydration as temperatures decrease in early winter (29, 35). The temporal separation of the HNO₃ and water removal processes could result if the large particles reported here also form in the Antarctic stratosphere before the onset of ice saturation temperatures. The more extensive low temper-

atures in the Antarctic suggest that large particles are formed there every winter, whereas their formation in the Arctic may not occur each year. Before the 1999/2000 Arctic observations, dilute populations of large particles in either vortex may have eluded detection because suitable instruments did not sample the vortices at the appropriate times and places.

By the end of March 2000, large ozone losses (up to 70% near 20 km) had occurred in the lower stratosphere throughout the Arctic vortex (23, 36). The significant level of denitrification observed throughout the vortex is expected to have enhanced the chemical loss (36). Arctic ozone abundances will remain vulnerable to increased winter/spring cooling in the polar vortex (37) and trends of increasing water vapor continue in the lower stratosphere (38). Both effects increase the extent of PSC formation and, thereby, denitrification and the lifetime of active chlorine (29). The role of large particles in effecting denitrification in these future scenarios is likely quite important. Substantial and widespread denitrification could possibly sustain chemical ozone loss in the Arctic even as total chlorine levels fall below 2 ppbv by 2070 (10). In this case, recovery of Arctic ozone would be delayed until chlorine levels decline further. Models of denitrification that accurately represent the formation of large particles will be required for accurate predictions and understanding of future ozone levels in the variable Arctic vortex.

Fig. 6. Growth calculation results for maximum NAT particle diameter as a function of sampling pressure, HNO₃ mixing ratio, and temperature (20). Particles are assumed to grow and sediment in a one-dimensional atmospheric model defined by a constant temperature of 188 or 190 K, an H₂O mixing ratio of 5 ppmv, and a given HNO₃ mixing ratio (horizontal axis). Particle growth occurs wherever NAT supersaturation conditions exist and, hence, begins at pressures between 13 and 23 hPa (25) for the highest and lowest HNO₃ mixing ratios, respectively, and extends down to the highest pressure shown (150 hPa). The solid curves indicate the constant HNO₃ mixing ratio and temperature values in the model that will produce the indicated particle diameter at a given pressure level (vertical axis). The horizontal dashed line is the ER-2 pressure level for sampling interval 2 in Fig. 2. NAD particles grow more slowly than NAT particles for the same HNO₃ partial pressure and, hence, would grow to smaller sizes (~20% less) for the same atmospheric conditions.



References and Notes

1. "Scientific Assessment of Ozone Depletion: 1998," Rep. 44 (World Meteorological Organization, Geneva, Switzerland, 1999).
2. S. Solomon, *Rev. Geophys.* **37**, 275 (1999).
3. Th. Peter, *Annu. Rev. Phys. Chem.* **48**, 785 (1997).
4. R. J. Salawitch et al., *Science* **261**, 1146 (1993).
5. R. W. Portmann et al., *J. Geophys. Res.* **101**, 22991 (1996).
6. O. B. Toon et al., *Geophys. Res. Lett.* **13**, 1284 (1986).
7. D. W. Fahey et al., *Nature* **344**, 321 (1990).
8. M. L. Santee, G. L. Manney, L. Froidevaux, W. G. Read, J. W. Waters, *J. Geophys. Res.* **104**, 8225 (1999).
9. C. P. Rinsland et al., *J. Geophys. Res.* **104**, 1847 (1999).
10. A. E. Waibel et al., *Science* **283**, 2064 (1999).
11. Y. Kondo, H. Irie, M. Koike, G. E. Bodeker, *Geophys. Res. Lett.* **27**, 337 (2000).
12. D. W. Fahey et al., *J. Geophys. Res.* **94**, 11299 (1989).
13. R. J. Salawitch, G. P. Gobbi, S. C. Wofsy, M. B. McElroy, *Nature* **339**, 525 (1989).
14. O. B. Toon, R. P. Turco, P. Hamill, *Geophys. Res. Lett.* **17**, 445 (1990).
15. The flights were part of the joint SAGE III Ozone Loss and Validation Experiment (SOLVE)/Third European Stratospheric Experiment on Ozone 2000 (THESEO 2000) campaigns that took place in Kiruna, Sweden, in the 1999/2000 winter (additional information on these campaigns is available at <http://cloud1.arc.nasa.gov/solve/> and www.nilu.no/projects/theseo2000/).
16. In addition to the NO_y instrument, a chemical ionization mass spectrometer (CIMS) detected HNO₃ in large PSC particles, and a multiangle aerosol spectrometer probe (MASP) measured the size and number concentration of large PSC particles (39). With

The Indian Ocean Experiment: Widespread Air Pollution from South and Southeast Asia

J. Lelieveld,^{1*} P. J. Crutzen,^{1,2} V. Ramanathan,² M. O. Andreae,¹
 C. A. M. Brenninkmeijer,¹ T. Campos,³ G. R. Cass,⁴
 R. R. Dickerson,⁵ H. Fischer,¹ J. A. de Gouw,⁶ A. Hansel,⁷
 A. Jefferson,⁸ D. Kley,⁹ A. T. J. de Laat,⁶ S. Lal,¹⁰
 M. G. Lawrence,¹ J. M. Lobert,² O. L. Mayol-Bracero,¹
 A. P. Mitra,¹¹ T. Novakov,¹² S. J. Oltmans,⁸ K. A. Prather,¹³
 T. Reiner,¹ H. Rodhe,¹⁴ H. A. Scheeren,⁶ D. Sikka,¹⁵ J. Williams¹

The Indian Ocean Experiment (INDOEX) was an international, multiplatform field campaign to measure long-range transport of air pollution from South and Southeast Asia toward the Indian Ocean during the dry monsoon season in January to March 1999. Surprisingly high pollution levels were observed over the entire northern Indian Ocean toward the Intertropical Convergence Zone at about 6°S. We show that agricultural burning and especially biofuel use enhance carbon monoxide concentrations. Fossil fuel combustion and biomass burning cause a high aerosol loading. The growing pollution in this region gives rise to extensive air quality degradation with local, regional, and global implications, including a reduction of the oxidizing power of the atmosphere.

Until recently, North America and Europe dominated the use of fossil fuels, resulting in strong carbon dioxide emissions and global warming (1). The fossil energy-related CO₂ release per capita in Asia is nearly an order of magnitude smaller than in North America and Europe (2). However, Asia is catching up. About half of the world's population lives in South and East Asia, and hence the potential for growing pollutant emissions is large. In China, many pollution sources reduce air quality (3–5). In rural residential areas, notably in India, the burning of biofuels, such as wood, dung, and agricultural waste, is a major source of pollutants (6). In urban areas, the increasing energy demand for industry

and transport propels fossil fuel utilization (7).

Here we evaluate measurements of the Indian Ocean Experiment (INDOEX) to characterize the atmospheric chemical composition of the outflow from South and Southeast Asia, from January to March 1999 during the dry winter monsoon (8). During this season, the northeasterly winds are persistent, and convection over the continental source regions is suppressed by large-scale subsidence, thus limiting upward dispersion of pollution (9). Our analysis is based on measurements from a C-130 and a Citation aircraft operated from the Maldives near 5°N, 73°E, the research vessels *Ronald H. Brown* and *Sagar Kanya*, and the Kaashidhoo Climate Observatory (KCO) on the Maldives (Fig. 1). During the campaign, the location of the Intertropical Convergence Zone (ITCZ) varied between the equator and 12°S. Hence, transport of primary pollutants and reaction products toward the ITCZ could be studied over an extended ocean area where pollutant emissions are otherwise minor. By performing measurements across the ITCZ, the polluted air masses could be contrasted against comparatively clean air over the southern Indian Ocean. Furthermore, we used the measurements to evaluate the numerical representation of these processes in a chemistry general circulation model (GCM) (10). The model was subsequently applied to calculate the large-scale atmospheric chemical effects of the measured pollution.

Aerosol chemical and optical measurements were performed from both aircraft, the *R/V Brown*, and KCO. The latter is located

the CIMS, air was sampled with an inlet specially designed to separate gas- and particle-phase HNO₃ by using a modified virtual impactor technique. During most flights, gas and particle phases were sampled alternately for periods of ~3 min each. The CIMS data confirm the NO_y component of the large particles as HNO₃ on 20 January and provide size and number concentration evidence consistent with the NO_y observations. With the MASP probe, the distribution of particles was measured for sizes from 0.3 to 22 μm in diameter on 20 January. The probe data confirm the presence of many small PSC particles between 0.3 and 2 μm and a few larger particles up to 20 μm in diameter. The probe data for the size and number of the larger particles are nominally consistent with the results in Fig. 4, although the statistical uncertainty is high because of low count rates. The number of particles in the size range of the small simulation mode in Fig. 4 is also nominally consistent with the probe data.

17. No direct measurements of particle shape are available. However, particles composed of solid HNO₃ hydrates are generally assumed to be nonspherical, even at sizes of <5 μm, because of lidar depolarization measurements [e.g., (40)]. Although modest corrections to fall speed and sampling efficiency calculations may ultimately be warranted because of nonspherical shapes, the assumption of sphericity is adopted here throughout for simplicity.
18. D. R. Worsnop, L. E. Fox, M. S. Zahniser, S. C. Wofsy, *Science* **259**, 71 (1993).
19. D. Hanson, K. Mauersberger, *Geophys. Res. Lett.* **15**, 855 (1988).
20. Supplementary material is available at www.sciencemag.org/cgi/content/full/291/5506/1026/DC1.
21. R. Müller, Th. Peter, *Ber. Bunsenges. Phys. Chem.* **96**, 353 (1992).
22. Denitrification is often observed with dehydration. Dehydration is rare in the Arctic vortex, whereas it is expected every winter in the Antarctic (7, 41). In the Arctic 1999/2000 winter, significant dehydration [up to 0.5 parts per million by volume (ppmv)] was observed at flight altitudes once during a brief period on a flight after 20 January.
23. M. Santee *et al.*, *Geophys. Res. Lett.* **27**, 3213 (2000).
24. G. L. Manney, J. L. Sabutis, *Geophys. Res. Lett.* **27**, 2589 (2000).
25. K. S. Carslaw, data not shown.
26. HNO₃ was observed remotely in the 5 to 8 km above the ER-2 aircraft by a microwave radiometer (42). The radiometer flew on board the NASA DC-8 aircraft during SOLVE/THESEO 2000.
27. T. Deshler *et al.*, *J. Atmos. Chem.* **30**, 11 (1998).
28. J. C. Wilson *et al.*, *Geophys. Res. Lett.* **17**, 361 (1990).
29. A. Tabazadeh *et al.*, *Science* **288**, 1407 (2000).
30. T. Koop *et al.*, *Geophys. Res. Lett.* **22**, 917 (1995).
31. U. M. Biermann *et al.*, *Geophys. Res. Lett.* **23**, 1693 (1996).
32. D. Hofmann, *Geophys. Res. Lett.* **17**, 369 (1990).
33. D. M. Murphy, D. S. Thomson, M. J. Mahoney, *Science* **282**, 1664 (1998).
34. S. C. Wofsy *et al.*, *Geophys. Res. Lett.* **17**, 449 (1990).
35. M. L. Santee *et al.*, *Science* **267**, 849 (1995).
36. B.-M. Sinnhuber *et al.*, *Geophys. Res. Lett.* **27**, 3483 (2000).
37. D. T. Shindell, D. Rind, P. Lonergan, *Nature* **392**, 589 (1998).
38. S. J. Oltmans, D. J. Hofmann, *Nature* **374**, 146 (1995).
39. D. Baumgardner *et al.*, *Geophys. Res. Lett.* **23**, 749 (1996).
40. E. V. Browell *et al.*, *Geophys. Res. Lett.* **17**, 385 (1990).
41. K. H. Rosenlof *et al.*, *J. Geophys. Res.* **102**, 13213 (1997).
42. H. Küllman *et al.*, in *Air Pollution Research Report 73*, N. R. P. Harris, M. Guirlet, G. T. Amanatidis, Eds. (European Commission, Brussels, 2000), pp. 699–702.
43. K. K. Kelly, *J. Geophys. Res.* **98**, 8713 (1993).
44. We appreciate the contributions of J. Barrilleaux, J. Nystrom, and D. Porter as NASA ER-2 pilots; of L. Lait in producing Fig. 1; and of B. P. Luo in discussions of the statistical evaluation of the particle size distributions. The NASA Upper Atmosphere Research Program supported this research.

7 November 2000; accepted 9 January 2001

¹Max-Planck-Institute for Chemistry, Post Office Box 3060, D-55020 Mainz, Germany. ²Center for Atmospheric Sciences, Scripps Institution of Oceanography, La Jolla, CA 92093–4922, USA. ³National Center for Atmospheric Research, Boulder, CO 80303, USA. ⁴School of Earth and Atmospheric Sciences, Georgia Institute of Technology, Atlanta, GA 30332–0340, USA. ⁵Department of Meteorology, University of Maryland, College Park, MD 20742, USA. ⁶Utrecht University, 3584 CC Utrecht, Netherlands. ⁷University of Innsbruck, A-6020 Innsbruck, Austria. ⁸Climate Monitoring and Diagnostics Laboratory, National Oceanic and Atmospheric Administration, Boulder, CO 80303, USA. ⁹Research Centre Jülich, ICG-2, D-52428, Jülich, Germany. ¹⁰Physical Research Laboratory, Navrangpura, Ahmedabad 380 009, India. ¹¹National Physical Laboratory, New Delhi 110 012, India. ¹²Lawrence Berkeley National Laboratory, Berkeley, CA 94720, USA. ¹³University of California, Riverside, CA 92521–0403, USA. ¹⁴Department of Meteorology, Stockholm University, S-10691 Stockholm, Sweden. ¹⁵40 Mausam Vihar, New Delhi 110051, India.

*To whom correspondence should be addressed. E-mail: lelieveld@mpch-mainz.mpg.de